In-situ ionothermally synthesized redox-active carbon nitrides-confined organic small molecule cathode for ultrastable lithium-ion batteries

Mingsheng Yang,[1] Rui Li,[2] Huige Ma,[2] Xiaoran Zhu,[2] Yan Wang,[3] Yuxin Hao,[2] Bei Wang,[2] Yucheng Dong,[5] Mingjun Hu,[1,] Jun Yang [2,4,*]*

1. School of Materials Science and Engineering, Beihang University, Beijing 100191, China;
2. Beijing Institute of Nanoenergy & Nanosystems, Chinese Academy of Sciences, Beijing 101400, China;
3. Center on Nanoenergy Research, School of Physical Science & Technology, Guangxi University, Nanning 530004, China;
4. ShenSi Lab, Shenzhen Institute for Advanced Study, University of Electronic Science and Technology of China, Shenzhen 518110, China;
5. South China Academy of Advanced Optoelectronics, International Academy of Optoelectronics at Zhaoqing, South China Normal University, Guangdong 510631, China.

* Corresponding authors:

mingjunhu@buaa.edu.cn, yangjun@binn.cas.cn

1. Experimental

1.1. Chemicals

Cyanuric chloride (250 g, 99 %), methanol (500 mL, AR 95 %), sodium hydroxide (500 g, 95 %), potassium chloride (500 g, AR 99.5%) and lithium Chloride (500 g, AR 99 %) were purchased from Macklin. $NH_2NH_2·H2O$ (80%) were purchased from Aladdin. These chemicals were used as received.

1.2. Materials preparation

1.2.1. The synthesis of 2,4,6-trimethoxy-1,3,5-triazine (TMTZ)

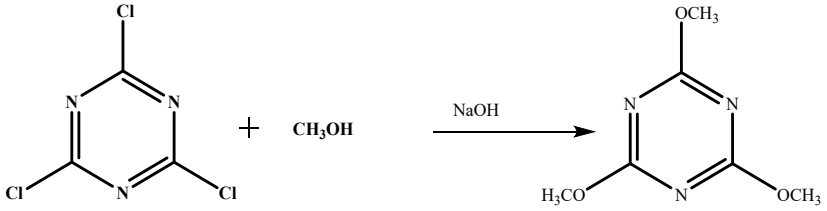

Scheme S1. The synthesis route for 2,4,6-trimethoxy-1,3,5-triazine.

Cyanuric chloride (92g, 0.5 mol) was added to the mixture of NaOH (60g, 1.5 mol) and methanol (500 mL) in small portions at a temperature of 0-5 ℃. After adding all the cyanuric chloride, the mixture was stirred at 20 ℃ for 4 h. The product was obtained by rotary evaporation, washed with deionized water, and freeze-dried, as shown in Scheme S1. The product was denoted as TMTZ.

1.2.2. The synthesis of 2,4,6-tris(hydrazino)-s-triazine (TH)

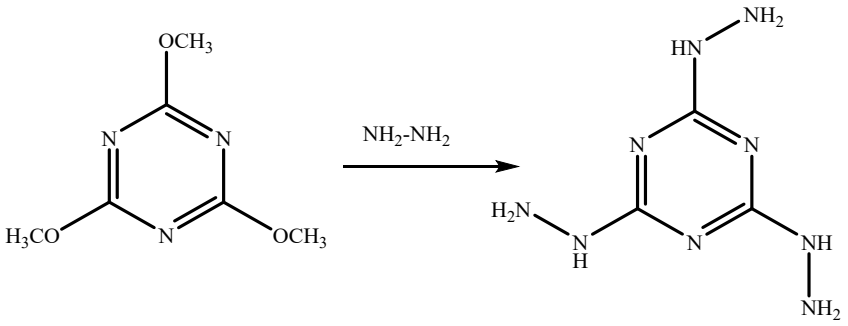

Scheme S2. The synthesis route for TH.

TMTZ (4 g, 23.3 mmol) was added to 300 mL of absolute ethanol, and then 37 mL of hydrazine hydrate was added drop by drop. The mixture was heated at 120 ℃ for 24 h. After the reaction was cooled to room temperature, a large number of solids were separated. After vacuum filtration, the crude product was washed with dichloromethane, dioxane, ethanol, and deionized water three times and then afforded

TH.

1.2.3. The synthesis of PTTH composites

Taking PTTH-3 as an example, TH (0.171g, 1 mmol), Perylene-3,4,9,10-tetracarboxylic dianhydride (PTCDA) (1.177g, 3 mmol), and 13.48 g of KCl/LiCl eutectic mixture were mixed by manually grinding for 10 min. Afterward, the mixture was transferred into a porcelain boat, heated at a temperature of 400 ºC with a ramping rate of 3 ºC min^{-1}, and kept at 400 ºC for 5 h at argon gas. The products/salt mixture was collected and thoroughly washed with methanol and deionized water. Finally, the products were obtained by vacuum drying at 120 ºC overnight. PTTH-1.5, PTTH-2, and PTTH-4 were obtained under the same condition, but adjusting the mole ratio of PTCDA to TH to be 1.5, 2, and 4, respectively. Moreover, the TH and PTCDA were treated under the same conditions, respectively noted as TH-400 and PTCDA-400, as control samples. PTTH-3-N_2 was prepared under the same condition as PTTH-3 without the addition of KCl-LiCl at 400 ℃ for 5 h under an atmosphere of nitrogen gas. The PTME was also prepared with the same condition as PTTH-3, except that TH is replaced by melamine. The preparation of NTTH-3 was similar to that of PTTH-3, but replacing PTCDA using 1,4,5,8-naphthalenetetracarboxylic dianhydride (NTCDA).

1.3. Materials characterization

Fourier Transform Infrared (FT-IR) spectrum was measured on a Thermo Scientific Nicolet iS50 spectrometer with Universal Attenuated Total Reflection (ATR) accessory (ZnS crystal) in the range of 400-4000 cm^{-1}. MALDI-TOF MS analysis was performed with an Ultraflex MALDI-TOF/TOF mass spectrometer (Bruker Daltonics, Germany) equipped with a nitrogen UV laser (337 nm) under the control of the software Flex Control 2.2. The ^{1}H and ^{13}C nuclear magnetic resonance (NMR) were conducted on a 600 MHz NMR spectrometer (Bruker, AscendTM 600 MHZ). Solid-state ^{13}C NMR were conducted on a 400 MHz NMR spectrometer (BRUKER AVANCE NEO 400WB). Material morphology was characterized by scanning electron microscopy (FEI Nova Nano SEM, American) and transmission electron microscopy (TEM, FEI Talos F200X; 200 kV) analyses. Thermogravimetric analysis (TGA) was performed

using a NETZSCH STA 449 F_5/F_3 Jupiter thermogravimetric analyzer at a ramping rate of 10 ℃ min^{-1} to 900 °C at the atmosphere of N_2. Differential Scanning Calorimeter (DSC) was performed using a NETZSCH STA 449 F_5/F_3 Jupiter thermogravimetric analyzer at a ramping rate of 10 ℃ min^{-1} to 500 °C at the atmosphere of N_2. X-ray photoelectron spectroscopy (XPS) was attained using Thermo Scientific Escalab 250Xi. The vibrational properties of materials were executed with Raman spectroscopy using were recorded on a LabRam HR Evolution; Horiba Scientific; renishaw inVa; Thermo Fischer DXR.

1.4. Electrode preparation

The working electrode was fabricated by mixing the electroactive materials, acetylene black and polyvinylidene fluoride (PVDF) with a mass ratio of 6:3:1 in N-methyl-2-pyrrolidone (NMP) to form a slurry, which was subsequently pasted on an Al foil and dried at 60 ℃ in a vacuum oven overnight. The mass loading of all electrodes is about 0.8-1.0 mg cm^{-2}. Electrode of NTCDA and NTTH-3 was fabricated by mixing the electroactive materials, acetylene black and polyvinylidene fluoride (PVDF) with a mass ratio of 6:2:2 in N-methyl-2-pyrrolidone (NMP) to form a slurry, which was subsequently pasted on an Al foil and dried at 60 ℃ in a vacuum oven overnight. The mass loading of all electrodes is about 1.2-1.4 mg cm^{-2} and 2-2.3 mg cm^{-2} for NTCDA cathode and NTTH-3 cathode, respectively. The normalization of electrochemical properties, such as current density of CV curve and specific capacity of CD curve, was estimated based on the total mass of composites (PTTH-1.5, PTTH-2, PTTH-3 and PTTH-4 or NTTH-3).

A pure lithium foil was used as both the counter and reference electrodes. 1.0 M $LiPF_6$ in ethylene carbonate/dimethyl carbonate (1:1 by vol) for was used as the electrolyte for PTCDA and PTTH-s. 1.0 M $LiPF_6$ in ethylene carbonate/diethyl carbonate (1:1 by vol) for was used as the electrolyte for NTCDA and NTTH-3. The polypropylene membrane (Celgard 2400) was used as a separator.

1.5. Characterization techniques

All electrochemical measurements were carried out using CR 2032 type coin cells assembled in an argon-filled glovebox (Etelux, Lab2000). The galvanostatic

charge/discharge tests of the assembled cells were carried out on a LANHE battery testing system (CT3001A) in the voltage range of 1.5-4 V for PTTH and TH-400, 1.5-3.5 V for PTCDA and PTCDA-400 at battery test incubator (BLC-300) with a constant temperature of 25 ℃. The cyclic voltammetry (CV) measurements were performed on an AMETEK-Princeton Applied Research electrochemical workstation. Electrochemical impedance spectroscopy (EIS) was also recorded on the electrochemical workstation with the frequency ranging from 10 mHz to 100 kHz at room temperature.

1.6 Calculation method

All calculations were performed with periodic DFT using the Gaussian plane wave method implemented in CP2K's Quickstep module.[1,2] The explorative studies of the catalysts structure were performed using the molecularly optimized basis set DZVP-MOLOPT-SR-GTH for each atom with a Goedecker-Teter-Hutter (GTH) pseudopotential.[3-6] The geometry optimizationwere conducted using the generalized gradient approximation and the Perdew-Burke-Ernzerhof (PBE) functional[7] with DFT-D3 correction[8,9] energy convergence for the self-consistent field (SCF) calculation was set to $2 \times 10{-}6$ Hartree. An energy cutoff of 400 Ry was used throughout the calculations. The input file was generated by Multiwfn.[10] In order to obtain more precise energy, the energy cutoff increased to 600 Ry and TZVP-MOLOPT-PBE-GTH basis set was employed when calculated single point energy. The HOMO-LUMO was calculated via Heyd–Scuseria–Ernzerhof (HES06) hybrid functional [11] with TZVP-MOLOPT-PBE-GTH combined Auxiliary Density Matrix Method (ADMM) basis set [12]. The binding energies (Ebind) are calculated using the follow equation:

$$E_{bind} = E_{PTCDA-xLi} - E_{PTCDA} - \mu_{Li}$$

$$E_{bind} = E_{C_3N_5-PTCDA-2Li} - E_{PTCDA-2Li} - E_{C_3N_5}$$

where E, and μ_{Li} stand for the energy of binding configurations or related model and the chemical potential of Li atom.

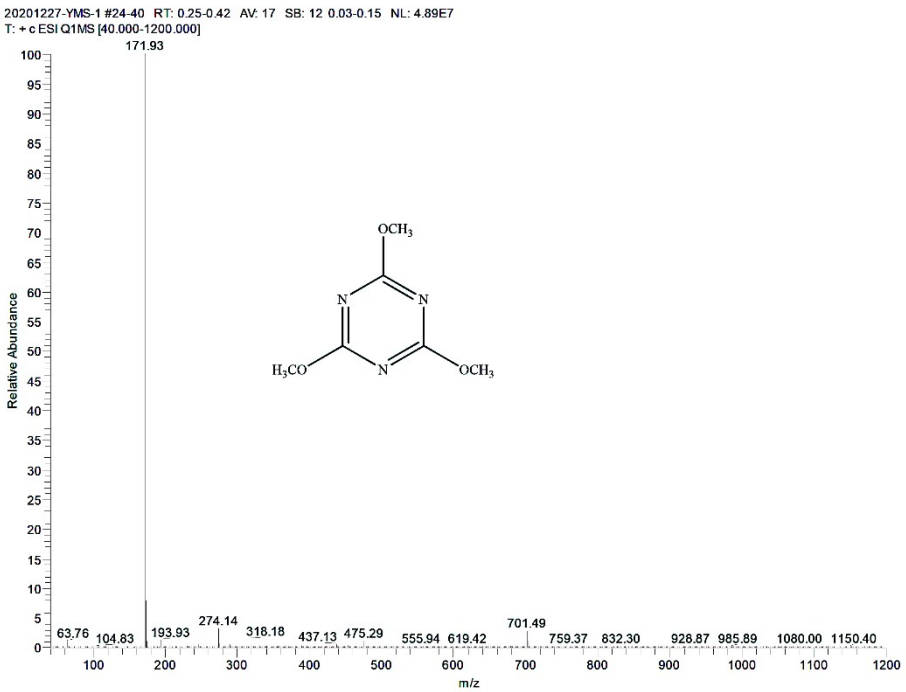

Figure S1. Mass spectrum of TMTZ.

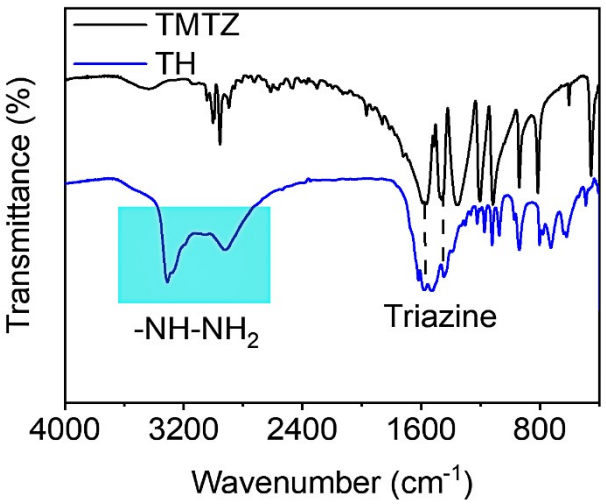

Figure S2. FT-IR spectra of TMTZ and TH.

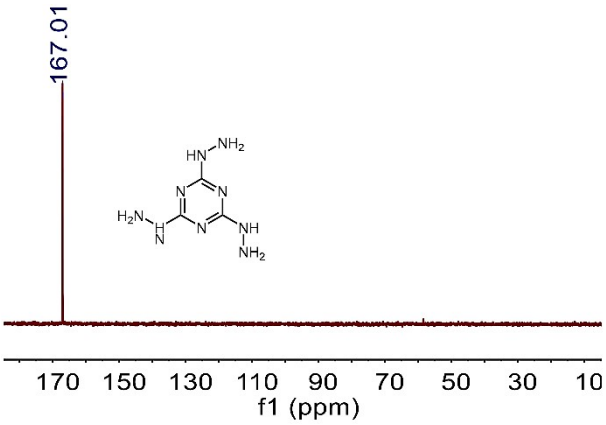

Figure S3. ^{13}C NMR spectra of TH.

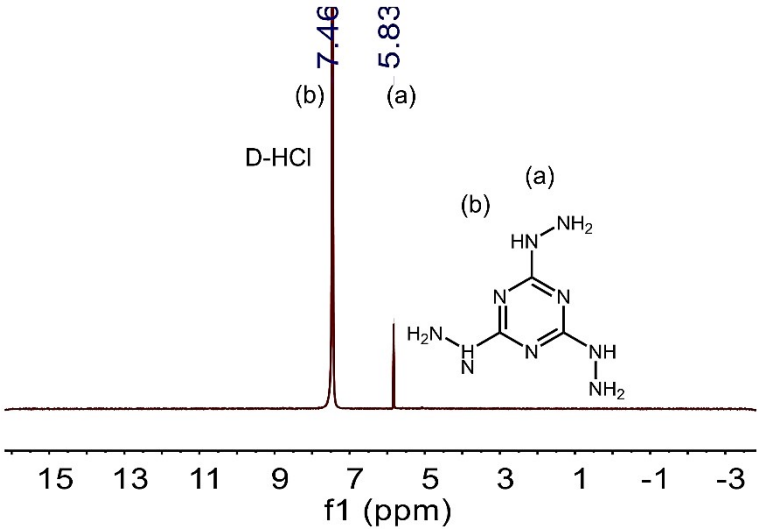

Figure S4. ^{1}H NMR spectra of TH.

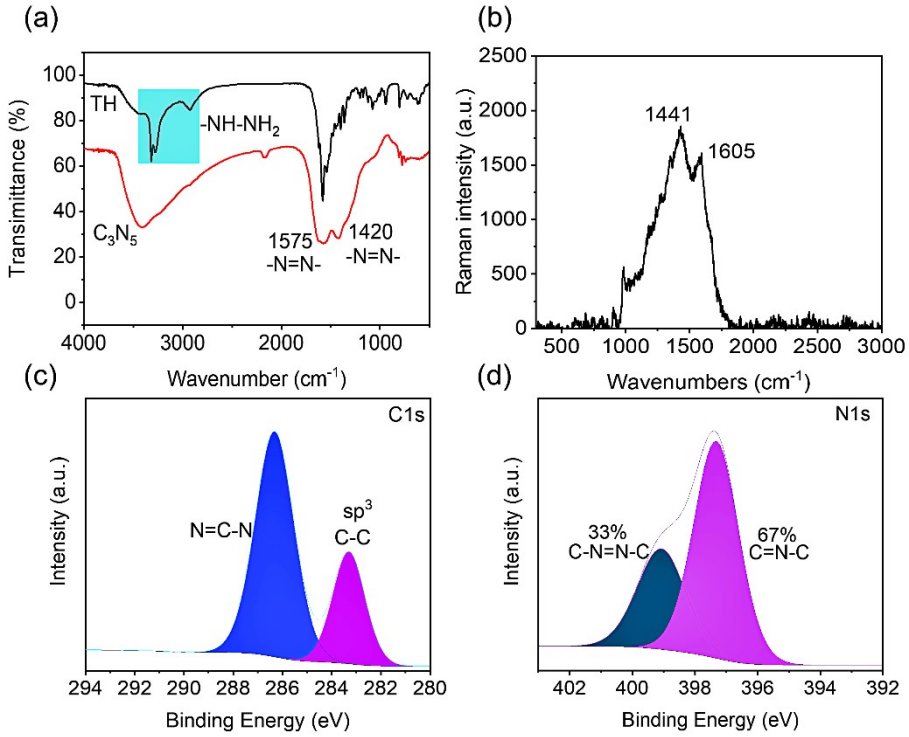

Figure S5. Structure characterization of C_3N_5: (a) FT-IR, (b) Raman, (c) C 1s XPS spectra, and (d) N 1s XPS spectra.

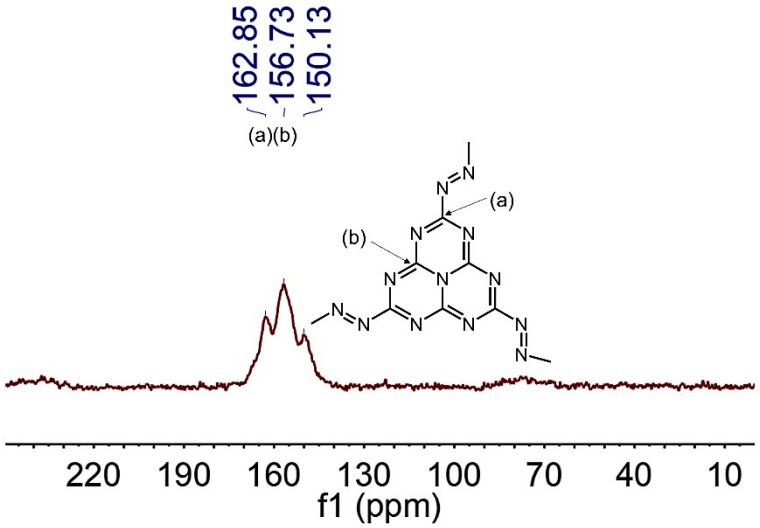

Figure S6. The solid-state ^{13}C cross-polarization magic angle spinning (CP/MAS) NMR spectrometry of C_3N_5.

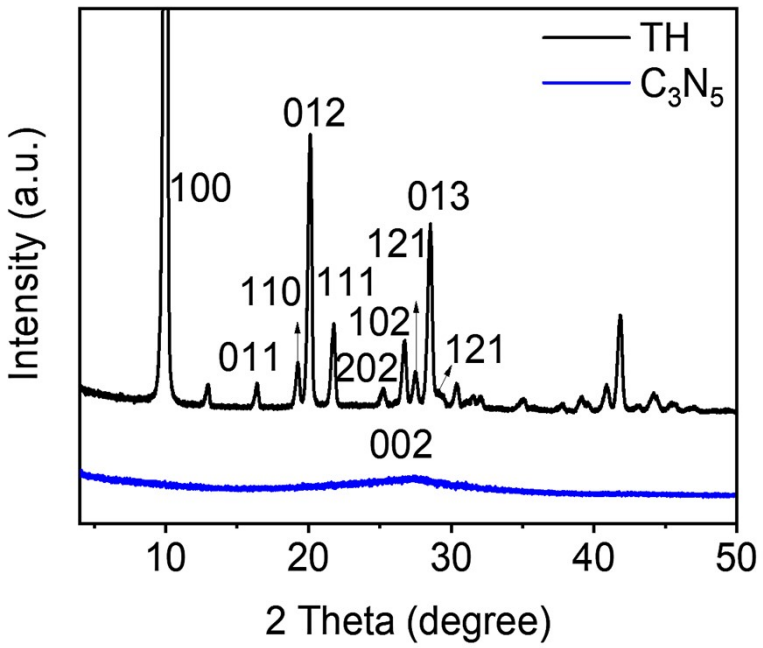

Figure S7. XRD patterns of TH and C_3N_5

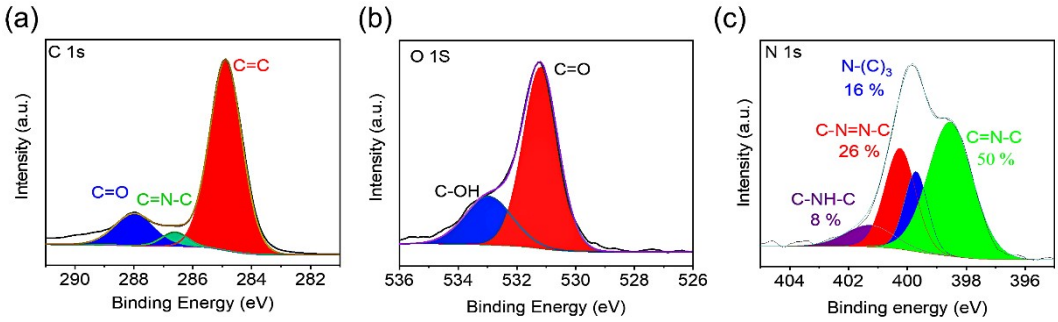

Figure S8. XPS spectra of PTTH-3

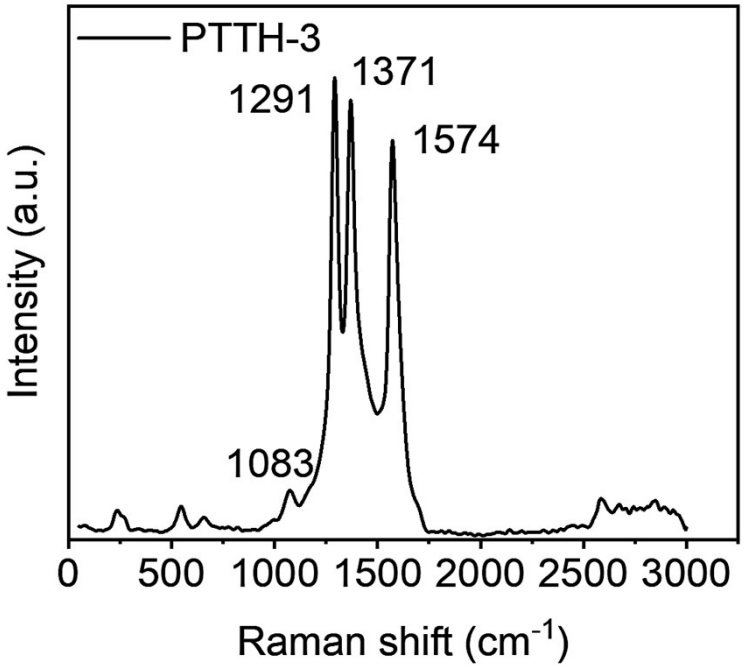

Figure S9. Raman pattern of PTTH-3.

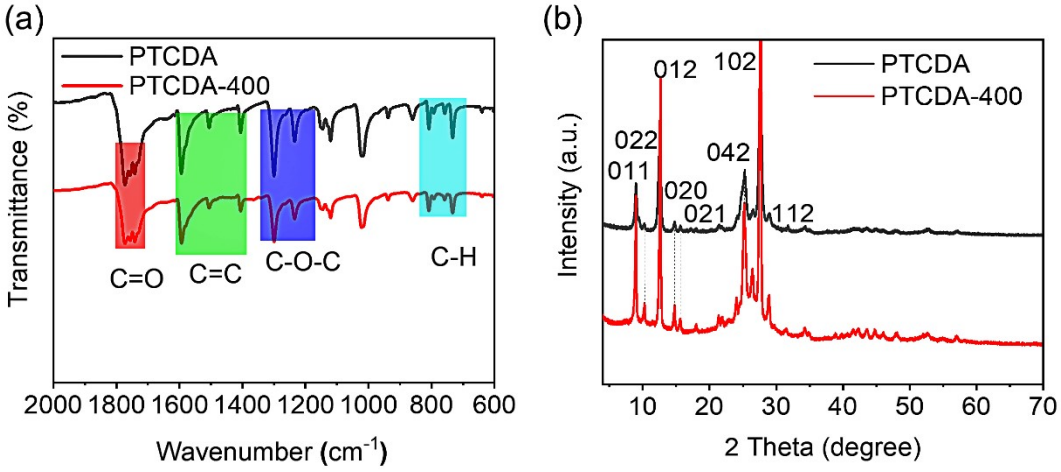

Figure S10. (a) FT-IR spectra and (b) XRD patterns of PTCDA and PTCDA-400.

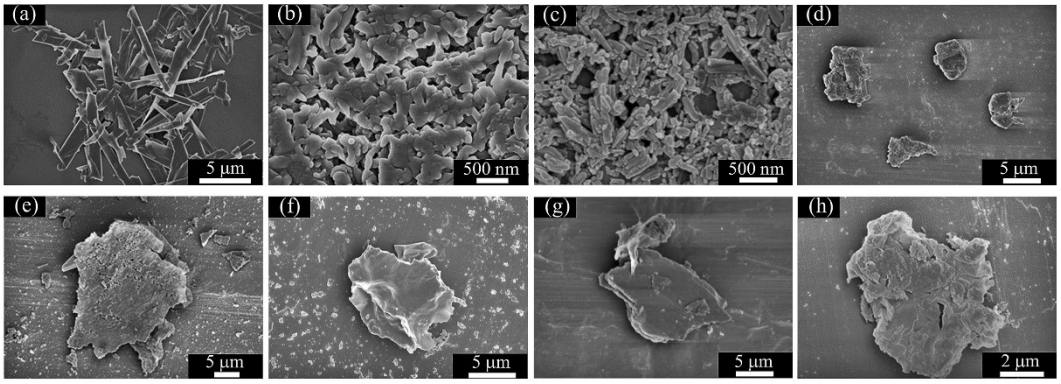

Figure S11. SEM images of (a) TH, (b) C_3N_5, (c) PTCDA, (d) PTCDA-400, (e) PTTH-1.5, (f) PTTH-2, (g) PTTH-3, and (h) PTTH-4.

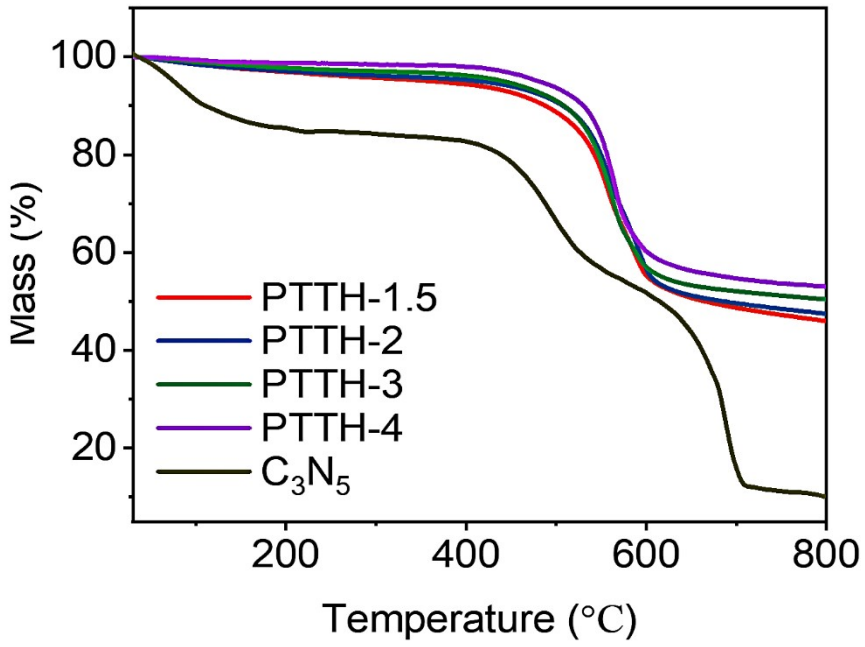

Figure S12. TG curves of C_3N_5, PTTH-1.5, PTTH-2, PTTH-3, and PTTH-4.

EIS was used to study the change in conducting properties of PTTH electrodes during charge-discharge cycling. As control samples, the resistance of PTCDA and PTCDA-400 showed a reduced trend (**Figure S13a and S13b**). It could be seen that the resistance of PPTH electrodes gradually decreased with increasing cycles (**Figure S13c-S13f**). As shown in Figure S13c-f, the resistance of PTTH-1.5, PTTH-2, PTTH-3, and PTTH-4 at open-circuit potential were 310, 400, 800, and 1100 Ω, respectively. After 300 cycles at 1 A g^{-1}, the resistance of PTTH-1.5, PTTH-2, PTTH-3, and PTTH-4 decreased to 25, 52, 130, and 105.3 Ω, respectively. When the cycling tests were extended to 2000 cycles, the resistance of PTTH-3 and PTTH-4 was further reduced to 12 and 74 Ω, respectively. This indicates that PTTHs' increase in conductivity upon reduction was not lost during charge-discharge cycling. In conclusion, all electrodes exhibited the bigger pristine resistance value in OCV, corresponding to lower kinetics. During the cycling process, the reaction resistance gradually decreases, which is attributed to the increased conductivity and optimized interface between the electrode and electrolyte.

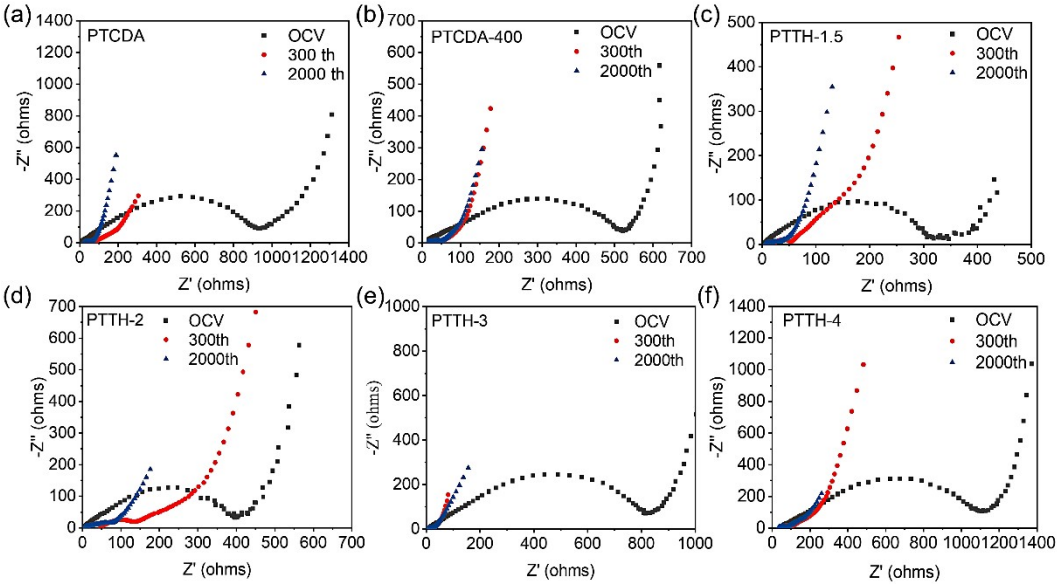

Figure S13. Nyquist plots of all samples in different cycles at 1 A g^{-1}.

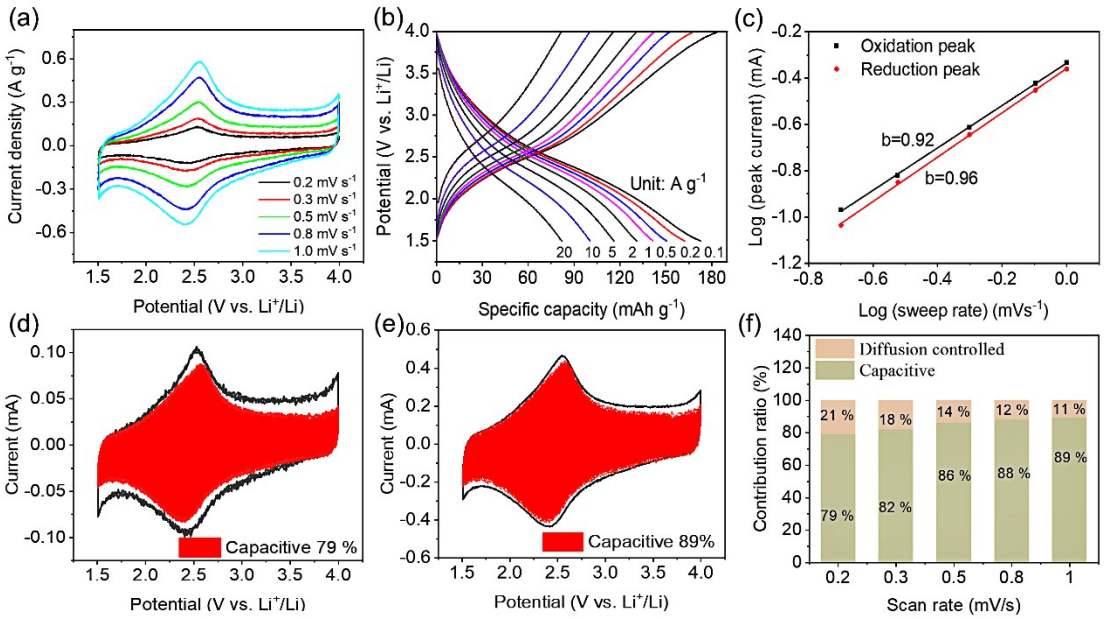

Figure 14. Electrochemical performance of PTTH-3 as the cathode materials for Li-ions batteries (LIBs). (a) CV curves at different scan rates, (b) Charge-discharge curves, (c) the corresponding plots of log (i) versus log (v) at each redox peak, (d) Capacitive behaviors and intercalation reaction contributions at 0.2 mV s^{-1}, (e) Capacitive behaviors and intercalation reaction contributions at 1 mV s^{-1}, and (f) Contribution ratio of the pseudocapacitance at various scan rates.

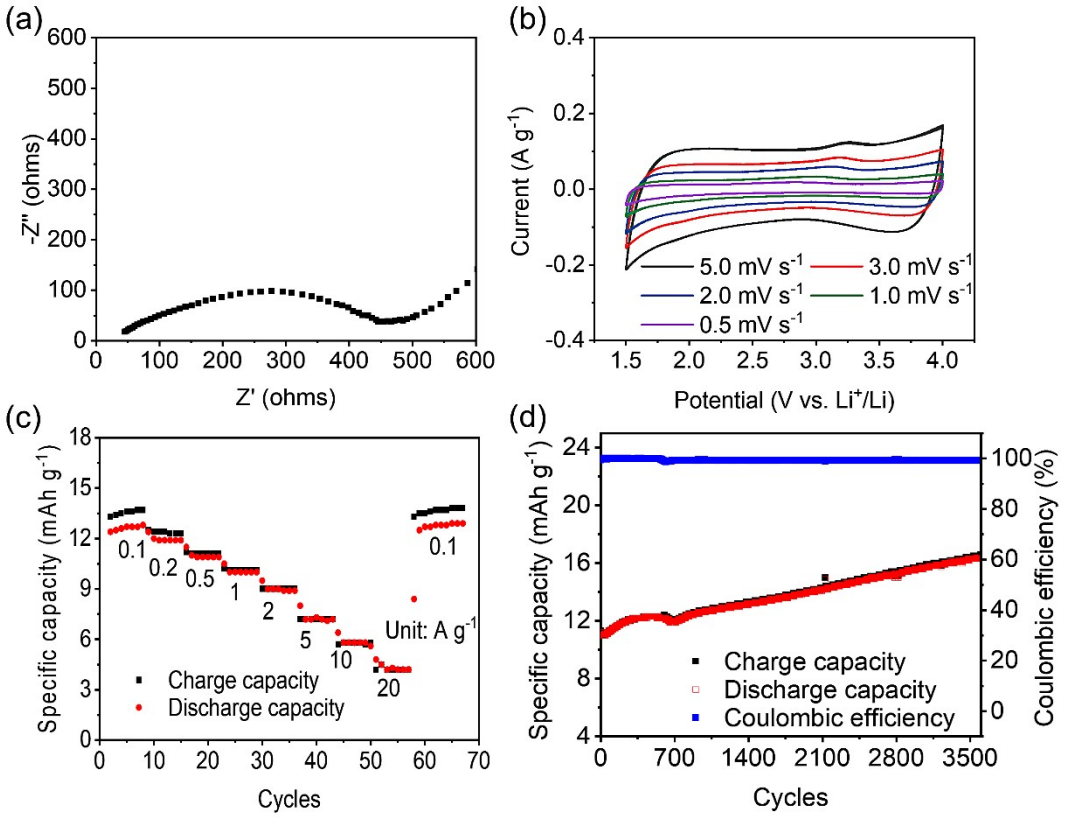

Figure S15. (a) Nyquist plots at the open-circuit potential for C_3N_5 at open-circuit voltage, (b) CV profiles of C_3N_5 at different scanning rates,(c) Rate performance of C_3N_5, and (d) Long-term cycling stability of C_3N_5.

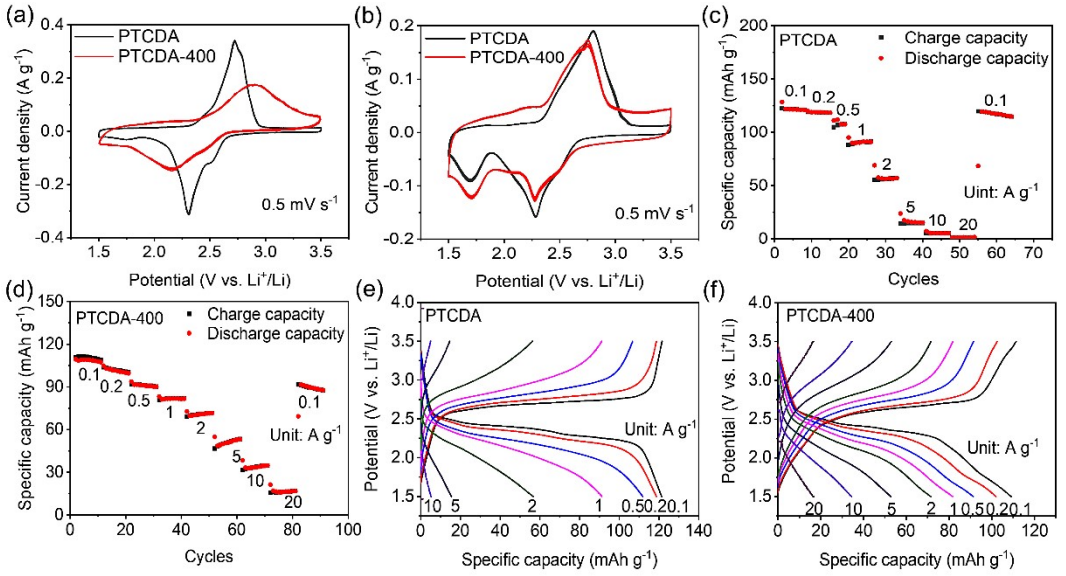

Figure S16. (a) CV profiles of PTCDA and PTCDA-400 at fresh rate, (b) CV profiles of PTCDA and PTCDA-400 after 300th at 1 A g^{-1}, (c) Rate performance of PTCDA, (d) Rate performance of PTCDA-400, (e) Charge-discharge curves for PTCDA, and (f) Charge-discharge curves for PTCDA-400.

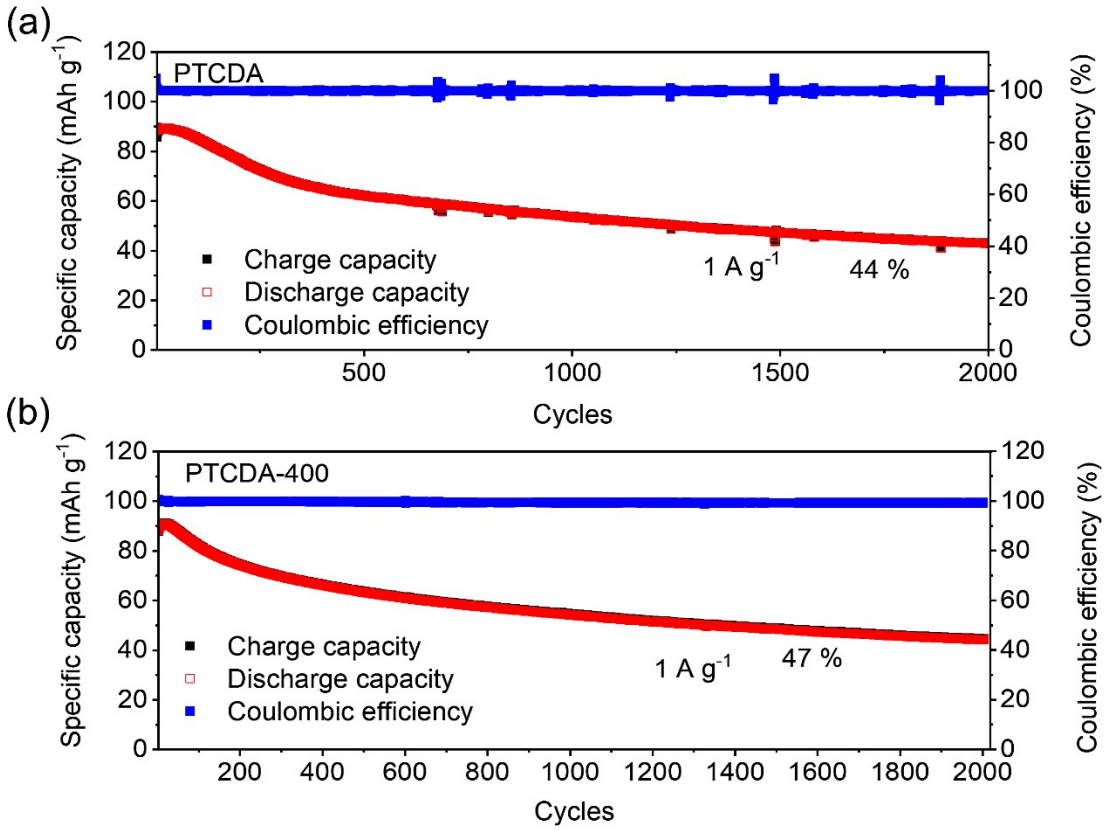

Figure S17. Long-term cycling stability of PTCDA and PTCDA-400 at 1A g^{-1}.

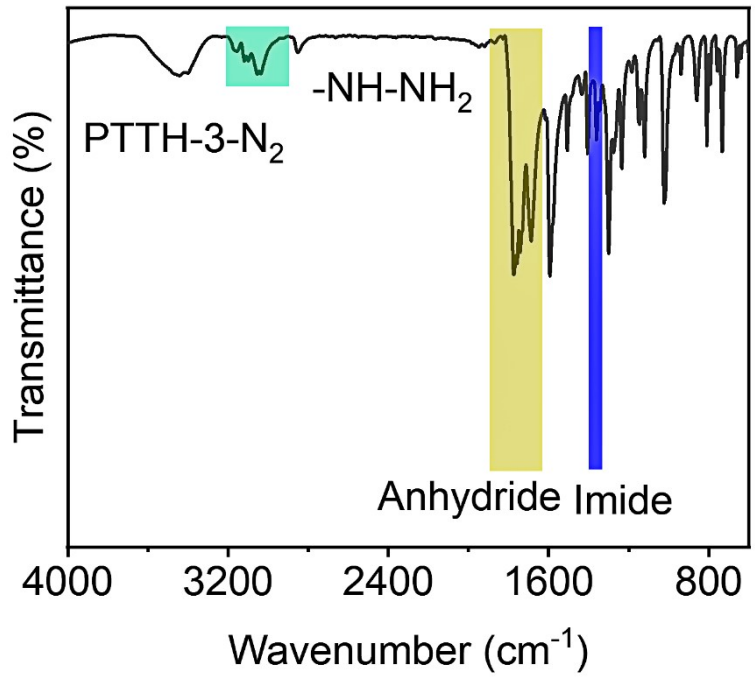

Figure S18 FT-IR spectra of PTTH-3-N_2.

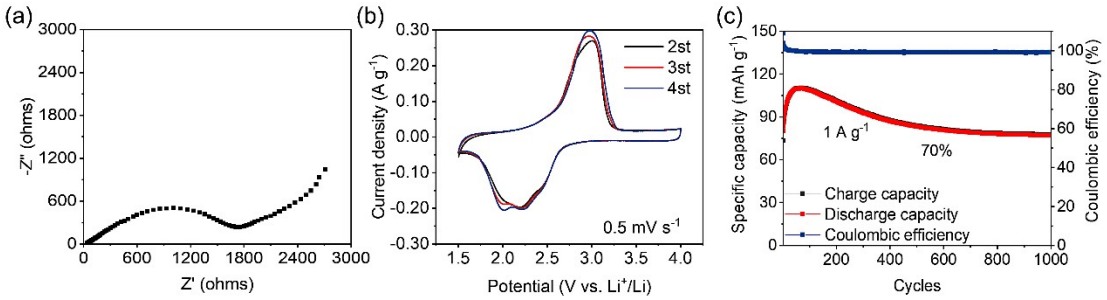

Figure S19. (a) Nyquist plots at the open-circuit potential for PTTH-3-N_2, (b) CV profiles of PTTH-3-N_2, and (c) Long-term cycling stability of PTTH-3-N_2.

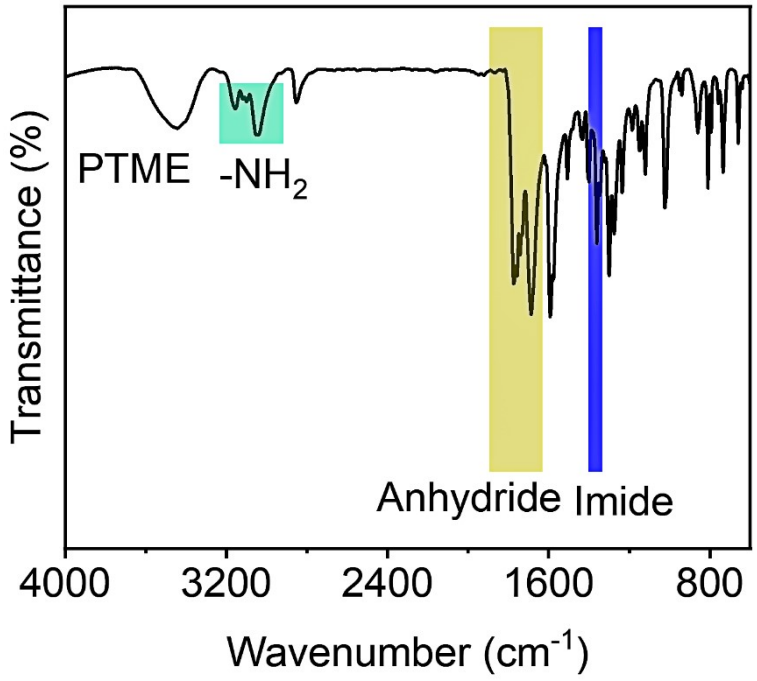

Figure S20. FT-IR spectra of PTME.

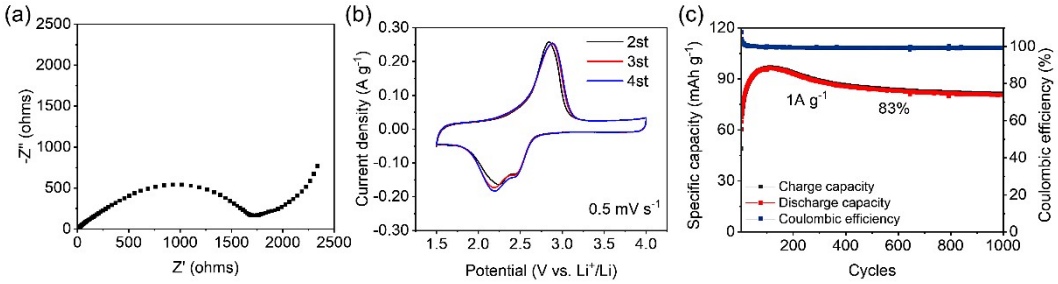

Figure S21. (a) Nyquist plots at the open-circuit potential for PTME, (b) CV profiles of PTME, and (c) Long-term cycling stability of PTME.

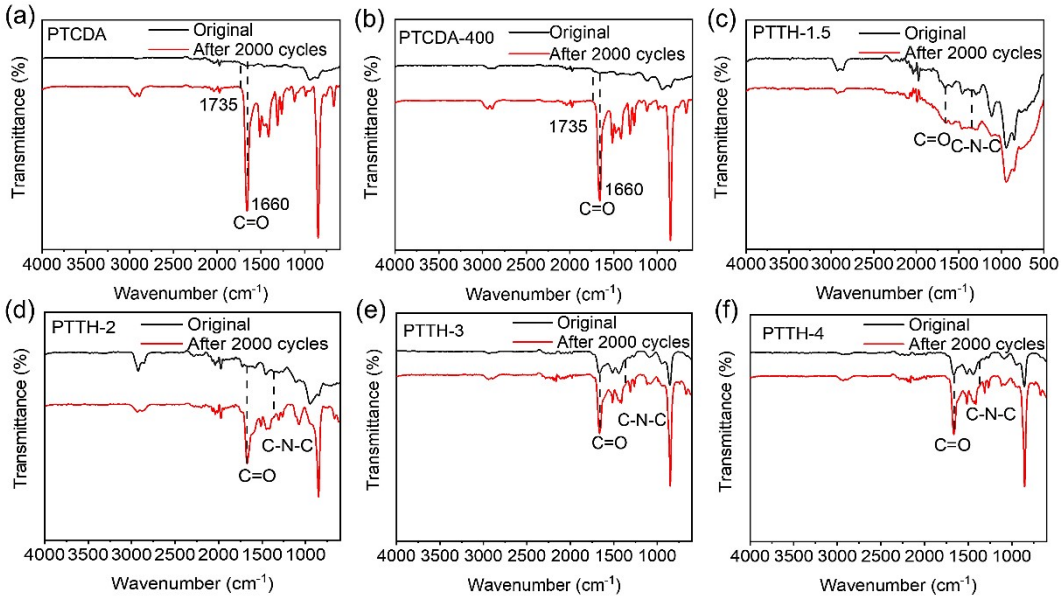

Figure S22. FT-IR spectra of samples at initial state and after 2000 cycles at 1A g^{-1}: (a) PTCDA, (b) PTCDA-400, (c) PTTH-1.5, (d) PTTH-2, (e) PTTH-3, and (f) PTTH-4.

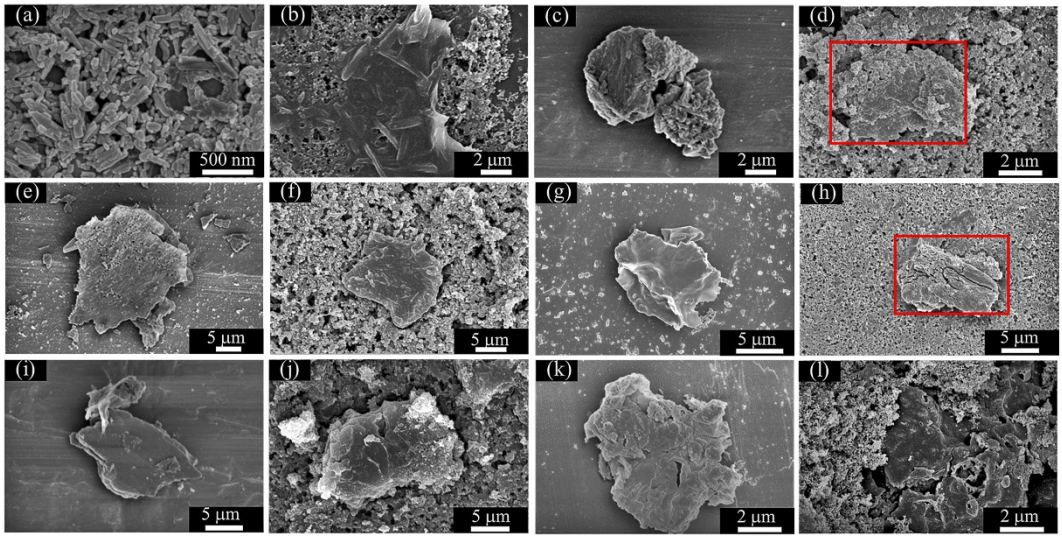

Figure S23. SEM images of (a) PTCDA, (b) PTCDA after 2000 cycles at 1A g^{-1}, (c) PTCDA-400, (d) PTCDA-400 after 2000 cycles at 1A g^{-1}, (e) PTTH-1.5, (f) PTTH-1.5 after 2000 cycles at 1A g-1, (g) PTTH-2, (h) PTTH-2 after 2000 cycles at 1A g^{-1}, (i) PTTH-3, (j) PTTH-3 after 2000 cycles at 1A g^{-1}, (k) PTTH-4, and (l) PTTH-4 after 2000 cycles at 1A g^{-1}.

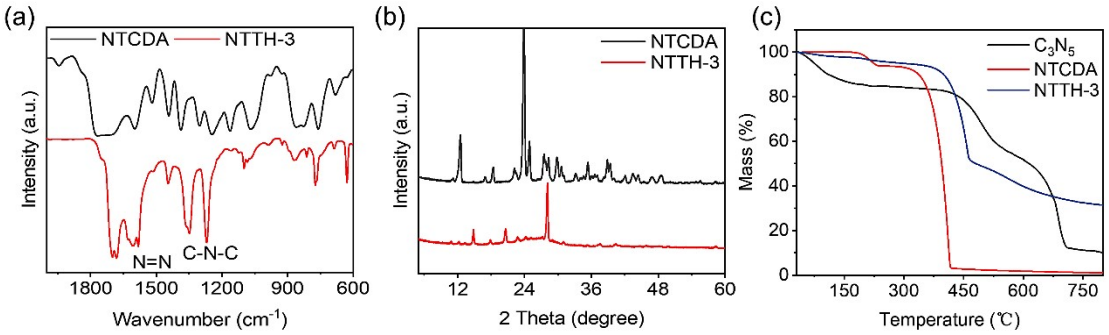

Figure S24. (a) FT-IR spectra of NTCDA and NTTH-3, (b) XRD patterns of NTCDA and NTTH-3, and (c) TGA curves of C3N5, NTCDA and NTTH-3.

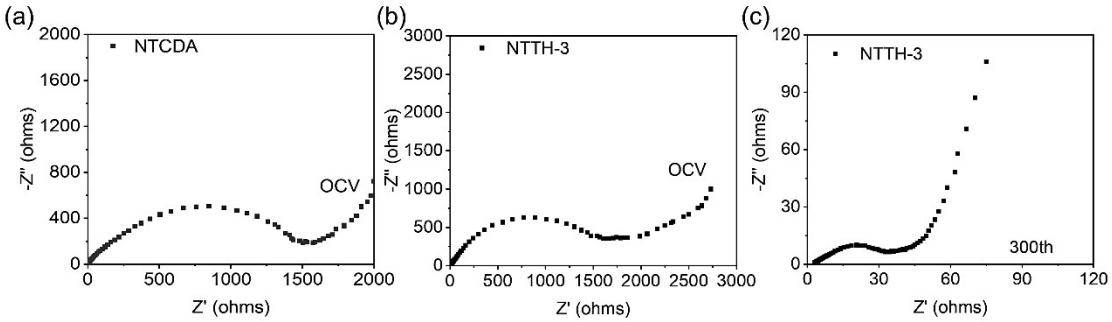

Figure S25. Nyquist plots of (a) NTCDA at open circuit voltage, (b) NTTH-3 at open circuit voltage, and (c) NTTH at 300th after 1 A g^{-1}.

Table S1. Elemental analysis of TH

	N (wt %)	C (wt %)	H (wt %)	N/C retio	Emperical formula
Theoretical value	73.65	21.05	5.3	2.9	$C_3N_9H_6$
Experiment value	72.86	21.21	5.23	2.9	$C_3N_9H_6$

Table S2. Elemental analysis of TH-400

	N (wt %)	C (wt %)	H (wt %)	N/C retio	Emperical formula
Theoretical value	66.02	33.98	0	2.9	C_3N_5
Experiment value	60.98	31.38	2.448	1.67	$C_3N_{5.10}H_{2.7}$

Table S3. Elemental analysis of PTTHs

	N (wt %)	C (wt %)	H (wt %)	O (wt %)
Theoretical value	17.87	66.39	2.14	13.60
Theoretical value	9.74	69.61	2.09	18.56
PTTH-1	10.2	68.54	2.384	19.453
PTTH-2	8.85	70.26	2.417	18.801
PTTH-3	6.51	69.07	2.441	20.155
PTTH-4	4.86	71.54	2.279	18.671

Table S4. The electronic conductivity of obtained samples.

Sample	Test content	Test methods	Results□			Units
□	□	□	2 MPa	4 MPa	6 MPa	□
C_3N_5	Electrical conductivity	Quadrupole probe	1.08 E^{-5}	1.38 E^{-5}	1.52 E^{-5}	S/m
PTCDA	Electrical conductivity	Quadrupole probe	4.53 E^{-7}	5.11 E^{-7}	6.77 E^{-7}	S/m

Comparison of performance with literature on organic cathode materials for LIBs

Table S5. Average discharge potential and cycling performance comparison of PTTH with other cathode materials reported in the literature.

Active compounds	Discharge capacity (mAh/g) /Current density (mA/g)	Cycling performance (Current density)	the mass of active material	the mass ratio of active material, carbon black, and PVDF/PTFE	Average discharge Voltage (vs.Li+ /Li /V)	Specific Energy (Wh/Kg)	Ref
DAPQ-COF	73/500	100%/After 400 cycles (500 mA/g)	0.3-0.6 mg/cm^2	6 3 1	2.56	184	13
2D CCP-HATN@CNT (50% CNT)	116/100	91%/After 1000 cycles (500 mA/g)	1 mg/cm^2	8 1 1	2.02	234	14
2D-PAI@CNT (50% CNT)	113/100, 100/1000	100%/After 8000 cycles (500 mA/g)	0.8-1.2 mg/cm2	8 11	2.48	287	15
DAAQ-TFP	16.9/3140	Less than 35%/After 500 cycles (157 mA/g)	0.8 mg/cm^2	6 1.5 1.5	2.2	161	16
E-TP-COF	50/1000	87%/After 500 cycles (200 mA/g)	0.9 mg/cm^2	6 3 1	/	/	17
CuPcNA-CMP	116.4/1000	60%/ After 500 cycles (1000mA/g)	/	4 5 1	/	/	18
PMTA/10.9 %SWCNT	140/383	100%/After 200 cycles (19.5 mA/g)	4 mg/cm^2	65 30 5	/	/	19
NTAQ	108.3/194	62%/After 1000 cycles (194 mA/g)	0.4 mg/cm^2	6 3 1	/	/	20
PTCDA@MXene	109.4/500	62.75%/After 1500 cycles (500 mA/g)	1.5 mg/cm^2	6 2 2			21
Cu-BHT MOF	133/1000, 100/2000	100%/After 500 cycles (1000 mA/g)	1.1-1.3mg/cm^2	7 2 1			22
PTCDA@GDY	138/100	93% /After 100 cycles (0.5C)	2 mg/cm^2		2.42	310	23

PTCDA	146/100	77%/After 1000 cycles (100 mA/g)		6 3 1			24
PTTH-1	118/100, 98/1000, 92/2000, 85/5000	100%/After 2000 cycles (1000 mA/g)	0.8-1.0 mg/cm^2	6 3 1	2.4	283	This work
PTTH-2	160/100, 120/1000, 118/2000, 100/5000	99.2%/After 2000 cycles (1000 mA/g)	0.8-1.0 mg/cm^2	6 3 1	2.4	384	This work
PTTH-3	173/100, 144/1000, 135/2000, 118/5000	97.5%/After 2000 cycles (1000 mA/g)	0.8-1.0 mg/cm^2	6 3 1	2.4	415	This work
PTTH-4	89.4/100, 84.7/1000, 80.2/2000, 71.3/5000	74.2%/After 2000 cycles (1000 mA/g)	0.8-1.0 mg/cm^2	6 3 1	2.4	215	This work

References:

1 T. D. Kuhne, M. Iannuzzi, M. Del Ben, V. V. Rybkin, P. Seewald, F. Stein, T. Laino, R. Z. Khaliullin, O. Schutt, F. Schiffmann, D. Golze, J. Wilhelm, S. Chulkov, M. H. Bani-Hashemian, V. Weber, U. Borstnik, M. Taillefumier, A. S. Jakobovits, A. Lazzaro, H. Pabst, T. Muller, R. Schade, M. Guidon, S. Andermatt, N. Holmberg, G. K. Schenter, A. Hehn, A. Bussy, F. Belleflamme, G. Tabacchi, A. Gloss, M. Lass, I. Bethune, C. J. Mundy, C. Plessl, M. Watkins, J. VandeVondele, M. Krack and J. Hutter, *Journal of Chemical Physics*, 2020, **152,** 194103.

2 J. VandeVondele, M. Krack, F. Mohamed, M. Parrinello, T. Chassaing and J. Hutter, *Computer Physics Communications*, 2005, **167**, 103-128.

3 M. Krack, *Theoretical Chemistry Accounts*, 2005, **114**, 145-152.

4 J. VandeVondele and J. Hutter, *Journal of Chemical Physics*, 2007, **127**.

5 G. Lippert, J. Hutter and M. Parrinello, *Molecular Physics*, 1997, **92**, 477-487.

6 C. Hartwigsen, S. Goedecker and J. Hutter, *Physical Review B*, 1998, **58**, 3641-3662.

7 J. P. Perdew, K. Burke and M. Ernzerhof, *Physical Review Letters*, 1997, **78**, 1396-1396.

8 S. Grimme, S. Ehrlich and L. Goerigk, *Journal of Computational Chemistry*, 2011, **32**, 1456-1465.

9 S. Grimme, J. Antony, S. Ehrlich and H. Krieg, *Journal of Chemical Physics*, 2010, **132**, 154104.

10 T. Lu and F. W. Chen, *Journal of Computational Chemistry*, 2012, **33**, 580-592.

11 J. Heyd, G. E. Scuseria and M. Ernzerhof, *Journal of Chemical Physics*, 2003, **118**, 8207-8215.

12 J. VandeVondele and J. Hutter, *Journal of Chemical Physics*, 2003, **118**, 4365-4369.

13 H. Gao, Q. Zhu, A. R. Neale, M. Bahri, X. Wang, H. F. Yang, L. J. Liu, R. Clowes, N. D. Browning, R. S. Sprick, M. A. Little, L. J. Hardwick and A. I. Cooper, *Adv. Energy Mater.*, 2021, **11**, 2101880.

14 S. Q. Xu, G. Wang, B. P. Biswal, M. Addicoat, S. Paasch, W. B. Sheng, X. D. Zhuang, E. Brunner, T. Heine, R. Berger and X. L. Feng, *Angew. Chem. Int. Edit.*, 2019, **58**, 849-853.

15 G. Wang, N. Chandrasekhar, B. P. Biswal, D. Becker, S. Paasch, E. Brunner, M. Addicoat, M. H. Yu, R. Berger and X. L. Feng, *Adv. Mater.*, 2019, **31**, 1901478.

16 E. Vitaku, C. N. Gannett, K. L. Carpenter, L. X. Shen, H. D. Abruna and W. R. Dichtel, *J. Am. Chem. Soc.*, 2020, **142**, 16-20.

17 G. F. Zhao, H. N. Li, Z. H. Gao, L. F. Xu, Z. Y. Mei, S. Cai, T. T. Liu, X. F. Yang, H. Guo and X. L. Sun, *Adv. Funct. Mater.*, 2021, **31**, 2101019.

18 X. X. Wang, W. Tang, Y. Hu, W. Q. Liu, Y. C. Yan, L. Xu and C. Fan, *Green Chem.*, 2021, **23**, 6090-6100.

19 H. P. Wu, Q. H. Meng, Q. Yang, M. Zhang, K. Lu and Z. X. Wei, *Adv. Mater.*, 2015, **27**, 6504-6510.

20 Z. H. Ba, Z. X. Wang, M. Luo, H. B. Li, Y. Z. Li, T. Huang, J. Dong, Q. H. Zhang and X. Zhao, *Acs Appl. Mater. Inter.*, 2020, **12**, 807-817.

21 C. L. Wei, L. W. Tan, Y. C. Zhang, B. J. Xi, S. L. Xiong and J. K. Feng, *Acs Appl. Mater. Inter.*, 2022, **14**, 2979-2988.

22 Z. Z. Wu, D. Adekoya, X. Huang, M. J. Kiefel, J. Xie, W. Xu, Q. C. Zhang, D. B. Zhu and S. Q. Zhang, *Acs Nano*, 2020, **14**, 12016-12026.

23 L. Li, Z. C. Zuo, F. Wang, J. C. Gao, A. M. Cao, F. He and Y. L. Li, *Adv. Mater.*, 2020, **32, 2000140**.

24 T. T. Cai, Y. Han, Q. Lan, F. Wang, J. Chu, H. Zhan and Z. P. Song, *Energy Storage Mater.*, 2020, **31**, 318-327.